arXiv:cond-mat/0409734v1 [cond-mat.mtrl-sci] 29 Sep 2004

First-principles characterization of ferromagnetic Mn_5Ge_3 for spintronic applications

S. Picozzi, A. Continenza
Center for Scientific and Technological Assistance to Industries (CASTI) - Istituto Nazionale di Fisica della Materia (INFM) and Dipartimento di Fisica, Università degli Studi di L'Aquila, I–67010 Coppito (L'Aquila), Italy

A.J.Freeman
Department of Physics and Astronomy, Northwestern University, Evanston, Il, 60208 USA

In the active search for potentially promising candidates for spintronic applications, we focus on the intermetallic ferromagnetic Mn_5Ge_3 compound and perform accurate first-principles FLAPW calculations within density functional theory. Through a careful investigation of the bulk electronic and magnetic structure, our results for the total magnetization, atomic magnetic moments, metallic conducting character and hyperfine fields are found to be in good agreement with experiments, and are elucidated in terms of a hybridization mechanism and exchange interaction. In order to assess the potential of this compound for spin–injection purposes, we calculate Fermi velocities and degree of spin–polarization; our results predict a rather high spin–injection efficiency in the diffusive regime along the hexagonal c-axis. Magneto-optical properties, such as $L_{2,3}$ X-ray magnetic circular dichroism, are also reported and await comparison with experimental data.

PACS numbers: 71.20.Lp,75.50.Cc,75.30.-m

INTRODUCTION

Mn–doped Ge has recently been proposed as a promising candidate in the challenging field of diluted magnetic semiconductors (DMS)[1, 2], which aims at combining information logic and storage. For example, epitaxial single crystal films of Mn_xGe_{1-x} ($x <$ 8-10%) grown on GaAs(001) and Ge were found to exhibit Curie temperatures over the range 25 to 116 K, combined with a p-type semiconducting behaviour[3]. Many efforts are presently devoted toward increasing the transition temperature up to or above room temperature. Within this framework, one possible way is to increase the concentration of magnetic impurities. However, one of the key issues in DMS is indeed the solubility of Mn in the semiconducting host: it is well known that beyond a certain critical Mn concentration (typically of the order of a few percent in III-V hosts), a tendency toward clustering and phase separation occurs, thereby limiting the homogeneity and growth control that are strictly required for materials to be used in spintronic applications. This tendency was observed also during Mn-alloying of Ge samples: Mn_xGe_y precipitates were detected during out-of-equilibrium growth[4].

Intermetallic compounds of Mn and Ge occur in several different stoichiometries and crystallographic phases[5], most of which are antiferromagnetic or ferrimagnetic with rather low ordering temperatures. However, Mn_5Ge_3 shows ferromagnetism with a Curie temperature of ∼300 K, along with a uniaxial magnetic anisotropy along the c axis of the hexagonal crystal structure (see below)[6, 7, 8]. Ferromagnetic Mn_5Ge_3 thin films grown epitaxially on Ge(111) by means of solid–phase epitaxy[8] exhibited metallic conductivity and strong ferromagnetism up to 296 K — thus holding out promise for use in spin injection. Moreover, very recently point contact Andreev reflection spectroscopy was used to measure the spin–polarization of Mn_5Ge_3 epilayers[9] and the results were compared with calculated values within the density functional theory. The discrepancy between the experimental and predicted spin–polarization was attributed to the extreme sensitivity of calculated results to the crystallographic structure, as well as to possible Mn deficiencies in Mn_5Ge_3 samples.[9] Finally, it was shown experimentally,[10] upon C doping (with carbon interstitially incorporated into the voids of Mn octahedra of the Mn_5Ge_3 compound), that the Curie temperature, T_C, dramatically increased: $Mn_5Ge_3C_x$ films for C concentration $x \geq 0.5$ showed $T_C \sim 680$ K.

So far, very little is known theoretically about Mn_5Ge_3 ; in particular, a careful investigation from first-principles of the magnetic interactions and chemical bonding between Mn and metalloid atoms is still lacking. In this work, we perform a comprehensive study of Mn_5Ge_3 within density functional theory; in particular, in Sec. we report the technicalities related to the structure and to the computational approach. The electronic structure, as well as the related magnetism, is discussed in Sec., in terms of band structure, orbital and spin magnetic moments, hyperfine fields and magnetic-circular dichroism spectra. Conclusions are drawn in Sec..

STRUCTURAL AND COMPUTATIONAL DETAILS

Our calculations were performed using one of the most accurate available density functional theory (DFT) methods, namely the all–electron full-potential linearized augmented plane wave (FLAPW) [11] approach. The

generalized gradient approximation (GGA) according to the Perdew-Becke-Erzenhof scheme[12] was used for the exchange-correlation (XC) potential. This choice was suggested by the more accurate treatment of this exchange–correlation functional for magnetic compounds with respect to the local spin-density approximation (LSDA)[13]; however, in order to test the resulting effects of a different (XC) parametrization and for the evaluation of the hyperfine fields, we also performed some calculations using the von Barth-Hedin[14] functional within the local spin density approximation (LSDA). We used plane waves with wave vector up to $K_{max} = 3.8$ a.u., leading to about 1500 basis functions, whereas for the potential and the charge density we used an angular momentum expansion with $l_{max} \leq = 8$. The Brillouin zone sampling was performed using 60 special k–points in the irreducible wedge, according to the Monkhorst-Pack scheme [15]. The muffin tin radii, R_{MT}, for Mn and Ge were chosen equal to 2.37 a.u. and 2.0 a.u., respectively. In order to evaluate the effects of the orbital contribution to the magnetic moments, the calculations were performed with and without the spin–orbit coupling (SOC) included in the Hamiltonian[16].

For the purpose of calculating the electronic group velocity $\mathbf{v}(\mathbf{k}) = (1/\hbar)[\partial\varepsilon(\mathbf{k})/\partial\mathbf{k}]$, the eigenenergies $\varepsilon(\mathbf{k})$ over a set of 150 $\mathbf{k}$ points were used for a spline fitting of the bands over the Brillouin zone [17]. The resulting interpolating Fourier series was then used to calculate the required energy derivative. A similar approach has been followed to calculate the electronic plasma frequency:

$$\omega^2_{p\alpha\beta} = \frac{4\pi e^2}{\Omega} N(E_F) < v_\alpha(\mathbf{k}) v_\beta(\mathbf{k}) > \qquad (1)$$

where $<>$ denotes the Fermi surface average. Given the hexagonal symmetry, the quantities, $\omega_{pxx} = \omega_{p\parallel}$ and $\omega_{pzz} = \omega_{p\perp}$, will be evaluated.

According to Forsyth and Brown[7], intermetallic Mn_5Ge_3 has an hexagonal crystal structure of $D8_8$ type (space group $P6_3/mcm$), with experimental cell dimensions at room temperature $a = 7.184$ Å and $c = 5.053$ Å. The atomic positions are:

Mn1 in 4(d) site: $\pm(\frac{1}{3}, \frac{2}{3}, 0; \frac{2}{3}, \frac{1}{3}, \frac{1}{2})$
Mn2 in 6(g) site: $\pm(x, 0, \frac{1}{4}; 0, x, \frac{1}{4}; -x, -x, \frac{1}{4})$ with $x = 0.2397$
Ge in 6(g) site: $\pm(x, 0, \frac{1}{4}; 0, x, \frac{1}{4}; -x, -x, \frac{1}{4})$ with $x = 0.6030$

Starting with the experimental equilibrium parameters, we checked that the calculated internal atomic forces were negligibly small and that the minimum total energy was obtained for the a and c value reported in Ref.7. This confirmed that the FLAPW method as well as the GGA parametrization accurately reproduce the experimental structural properties for compounds with a high concentration of magnetic atoms. In Figure 1, we show

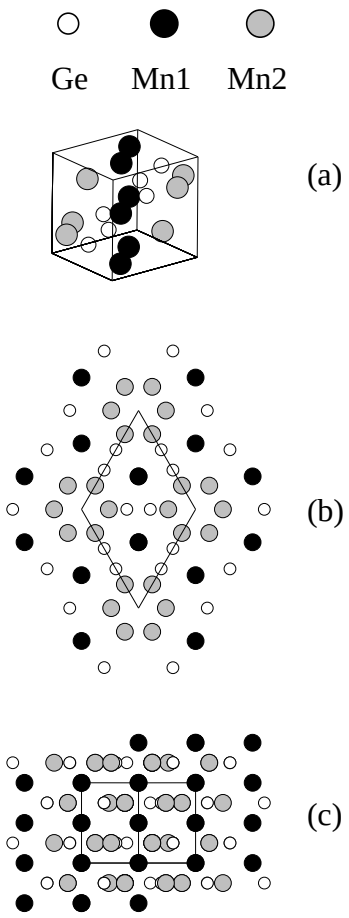


FIG. 1: (a) Perspective, (b) top and (c) side views of Mn_5Ge_3. Black, white and grey spheres denote Mn1, Ge and Mn2 atoms. The unit cell is also shown.

the perspective, top and side views of the crystal. It is evident that there are two different atomic planes perpendicular to the [001] direction: the first contains only Mn1 atoms (at $z = 0$ and $z = c/2$, equivalent by symmetry) forming an hexagonal two-dimensional lattice; the second contains Mn2 and Ge atoms (at $z = c/4$ and $z = 3c/4$, equivalent by symmetry). We recall that in the complex Mn_5Ge_3 structure, Mn1 and Mn2 atoms have different coordinations; in particular[7], the nearest neighbours (nn) of each Mn atoms are arranged as:

- Mn1 has (i) two (six) Mn1 (Mn2) nearest-neighbors at 2.522 (3.059) Å and (ii) six Ge at 2.534 Å;
- Mn2 has two Mn2, four Mn2 and four Mn1 at 2.976, 3.051 and 3.059 Å, respectively and (ii) two Ge, one Ge and two Ge at 2.482, 2.606 and 2.762 Å, respectively.

In this configuration, the enthalpy of formation, ΔH_f, of Mn_5Ge_3 is evaluated with respect to the stable phases of Mn ([001]-ordered antiferromagnetically fcc) and Ge (in the zincblende phase). Our GGA calculated value,

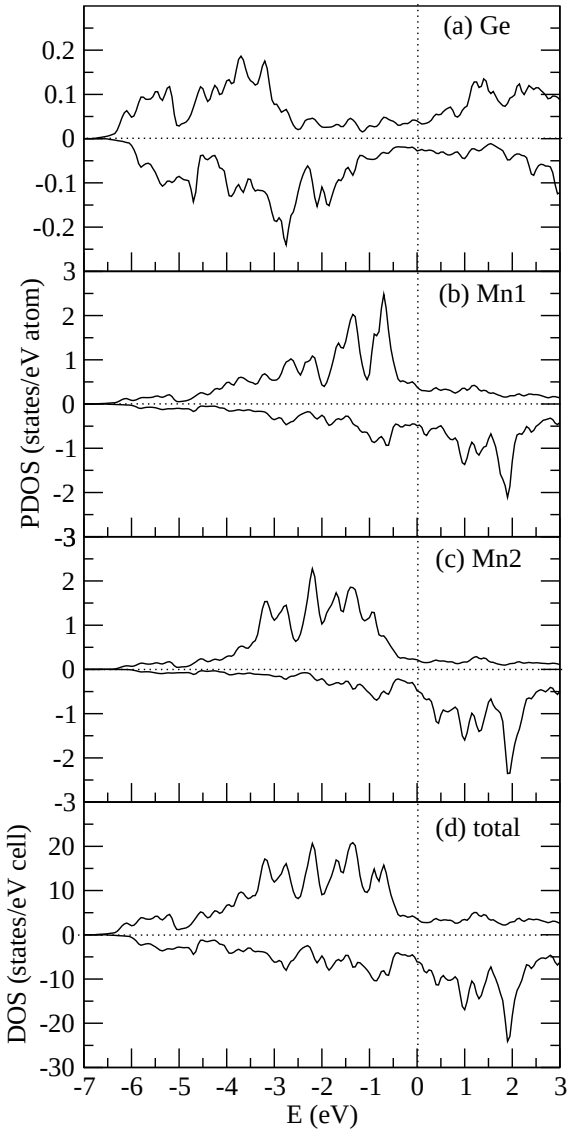


FIG. 2: PDOS of (a) Ge, (b) Mn1 and (c) Mn2 the total density of states is shown in panel (d). Majority (minority) spin components are shown in the positive (negative) y-axis. The E_F is set to zero of the energy scale.

$\Delta\ H_f$ = 0.84 eV/formula–unit (*i.e.* ∼0.1 eV/atom), shows that Mn_5Ge_3 is a quite stable compound.

ELECTRONIC AND MAGNETIC PROPERTIES

Density of states and band structure

The projected density of states (PDOS) of the three different atomic types forming the unit cell and the total DOS are reported in Figure 2. As for its conducting character, Mn_5Ge_3 shows strongly metallic behavior in both the minority and majority spin components: this is consistent with recently reported electrical resistivity experiments[8]. The Ge atom shows slightly different PDOS for up and down spins, consistent with the small negative magnetic moment (see below). In the energy range considered, the largest contribution is due to p states. On the Mn sites, as expected, contributions from s and p states (not shown) are negligible and the PDOS is essentially dominated by the $3d$ states. As a difference with the case of Mn impurities in Ge[18], we here have a much smaller hybridization between Ge p and Mn d states. In fact, we find the Ge p states at higher binding energy while the Mn d dominate the region close to the Fermi level, showing a quite large Mn–Mn interaction.

Differences in the PDOS of Mn1 and Mn2 are particularly evident in the majority spin occupied states; in particular, from the analysis of the peaks on different atoms located at the same energies, we can infer that: *i*) the Mn1 features at ∼-0.7 eV and in–between -2 and -3 eV are due to Mn1–Mn1 interactions; *ii*) the feature at ∼-1-2 eV is due to Mn1-Mn2 interactions; *iii*) the Mn2 feature at -3.5-2.5 eV can be ascribed to Mn2-Mn2 interactions. The high–binding energy range (<-3.5 eV) shows hybridization of both Mn atoms with Ge. Similarly, minority states for binding energies greater than 1.3 eV show common features for Mn1, Mn2 and Ge atoms, whereas the feature at around -1-0.5 eV results from Mn1-Mn2 hybridization. The unoccupied states, of interest for the discussion of magneto-optical properties (see below), are largely due to the minority spin component and only show minor differences between Mn1 and Mn2.

The band structure for the majority and minority spins is shown in Figure 3. We remark that the levels around E_F (see Figure 3 (b) and (d)) are rather dispersed for the majority spin channel, whereas they are more localized in the minority spin component; moreover, a non–dispersed region is evident for higher binding energies in the majority spin band structure (in the energy range from -0.7 eV to -3.5 eV), as well as in the unoccupied minority spin band structure. The dispersion around E_F in the up-spin component confirms the strong hybridization between Mn1 and Mn2 states, and between Mn d and p Ge states. Roughly speaking, in fact, as already pointed out for the DOS, the region at higher binding energies (*i.e.* in the energy range between -7 eV and -1.5 eV) is basically due to a large contribution from Ge; on the other hand, the levels around E_F are basically due to both Mn1 and Mn2 in the minority spin channel, whereas a p Ge contribution hybridized with Mn states is evident in the majority spin bands.

Magnetic moments, spin and charge density

The calculated total magnetization and the magnetic moments of the different atomic species are compared with their corresponding experimental values and re-

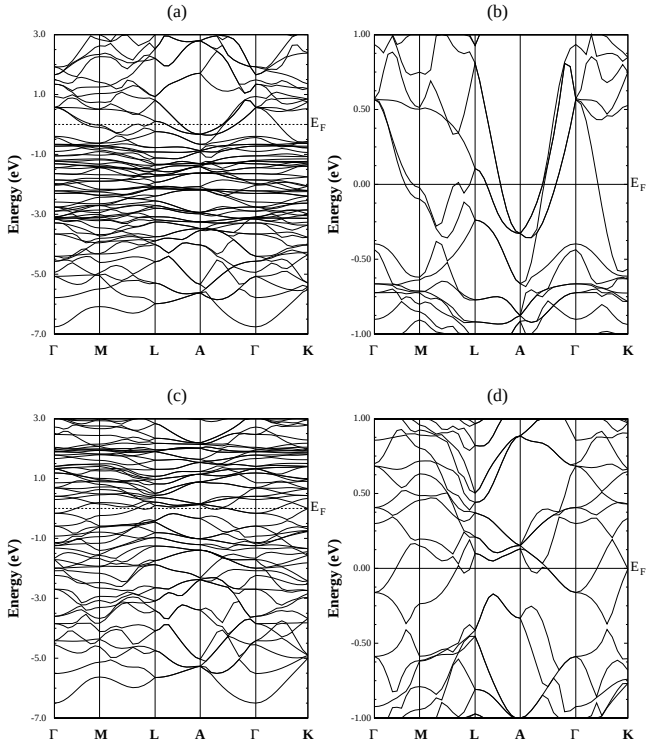


FIG. 3: (a) Majority and (c) minority band structure along the main symmetry lines. Panels (b) and (d) show a blow-up around the Fermi level. The E_F is set to zero of the energy scale.

TABLE I: Magnetic moments within the atomic spheres and total magnetization per unit cell (in Bohr magnetons). The first two lines show the spin magnetic moments (μ^s_{NOSOC}) as obtained from calculations without SOC within LSDA and GGA; the third, fourth and fifth lines show the spin (μ^s_{SOC}), orbital (μ^l_{SOC}) and total (μ^t_{SOC}) magnetic moments as obtained including the SOC self-consistently within GGA. The magnetic moments of the atomic species are calculated within their muffin-tin spheres, whereas the total contribution includes the contribution from the interstitial region. Experimental values (μ^t_{exp}) from Refs.7, 8 are shown in the last row.

	Ge	Mn1	Mn2	Total
μ^s_{NOSOC} (LSDA)	-0.09	2.14	3.11	26.7
μ^s_{NOSOC} (GGA)	-0.11	2.28	3.22	27.5
μ^s_{SOC} (GGA)	-0.11	2.07	3.12	-
μ^l_{SOC} (GGA)	0	0.05	0.035	-
μ^t_{SOC} (GGA)	-0.11	2.12	3.16	25.9
μ^t_{exp}	-	1.96[a]	3.23[a]	26[b]

a. Ref.7
b. Ref.8

ported in Table I. We show the magnetic moments (both spin and orbital contributions) with and without the inclusion of SOC. As experimentally reported[7], all the moments are ferromagnetically oriented along the crystallographic c axis. A comparison between LSDA and GGA does not show any significant differences as far as the general magnetization distribution over different atomic sites is concerned; however, LSDA predicts lower atomic magnetic moments (by about 0.1-0.15 μ_B) than GGA, resulting in a LSDA total magnetic moment per unit cell that differs by almost one Bohr magneton with respect to its GGA counterpart.

According to previous neutron scattering experiments[19], the magnetic structure of Mn_5Ge_3 is found to reveal two Mn sublattices (Mn1 in a four-fold and Mn2 in a six-fold position) with different magnetic moments. It was suggested that Mn2 carries the larger moment, in agreement with zero-field NMR measurements[20]. Our results are in excellent quantitative and qualitative agreement with these results. As suggested in Ref.7, the lower Mn1 magnetic moment is due to the different Mn coordination and to direct Mn–Mn interactions at a rather short distance (recall, in fact, that every Mn1 atom in Mn_5Ge_3 has 2 Mn1 at a distance of 2.52 Å): for a large set of Mn intermetallic compounds, an analysis of the Mn magnetic moment vs the nearest neighbor distance[7] showed that below a "threshold" separation of 3.1 Å, a moment reduction of $\sim$ 2 μ_B/Å per Mn neighbor occurred with respect to the atomic value (5 μ_B) of the Mn^{2+} ion, therefore accounting for the small magnetic moment at the Mn1 site.

It is remarkable that the inclusion of the orbital moments (which are not completely negligible on both the Mn1 and Mn2 sites) largely improves the agreement with experiment: the total magnetic moment is in excellent agreement with the experimental saturation magnetization as obtained by Kappel[21]. Moreover, it was suggested by Forsyth and Brown[7] that some *spatially diffuse* reverse magnetization (in contrast to *localized* moments centered on the Mn atoms) exists in Mn_5Ge_3. This is consistent with our calculated negative moment on Ge sites. As expected, the Mn magnetic moments are due to d states, whereas the small induced moment on Ge is due to p state polarization. In order to further investigate this issue and to better show the bonding, we plot the charge and spin density on two different planes perpendicular to the [0001] axis. The charge density in Figure 4 (a) shows fairly "isolated" Mn1 atoms; a somewhat stronger interaction occurs between Ge and Mn2 atoms, as shown by the presence of charge in the bonding regions in Figure 4 (c).

As regards deviations from spherical symmetry in the spin density, we remark that Mn2 shows an almost spherical shape, whereas the spin density around Mn1 is extended towards the six surrounding Ge ligands. It is ev-

FIG. 4: (a) Valence charge density and (b) spin density in a plane perpendicular to the [0001] direction and containing Mn1 atoms. (c) Valence charge density and (d) spin density in a plane perpendicular to the [0001] direction and containing Mn2 and Ge atoms. Shading for the atomic spheres are consistent with Figure 1: white, black and grey circles denote Ge, Mn1 and Mn2 atoms, respectively. In panels (b) and (d) solid (dashed) lines show the positive (negative) contribution to the spin density.

ident from Figure 4(d) that a negative spin-density surrounds the metalloid Ge atoms, consistent with the negative magnetic moment reported in Table I. Moreover, the *diffuse* negative spin density shown in Figure 4 (b) and (d) confirms the experimental results.[7]

Hyperfine fields

We focus next on hyperfine fields and compare our predicted values with experimental data[20]. As is well-known, the hyperfine field[22] of an atom is the magnetic field at the atomic nuclear site produced by the electrons in the solid and can be probed using Mössbauer spectroscopy or nuclear magnetic resonance to provide valuable information on the electronic and magnetic properties of the compound. It consists of several contributions: (i) the leading term due to the Fermi contact interaction which is proportional to the spin density at the nucleus[22],

$$H_{hf}^{ct} = \frac{8}{3}\pi\mu_B^2[\rho_\uparrow(0) - \rho_\downarrow(0)], \tag{2}$$

in the scalar relativistic limit; (ii) an orbital term which, according to Abragam and Pryce[23] can be expressed as:

$$H_{hf}^{orb} \sim 2\mu_B < r^{-3} >_l \mu^l \tag{3}$$

where $< r^{-3} >_l$ is the average expectation value of r^{-3} of the radial wave function and μ^l is the orbital magnetic moment; (iii) a dipolar term H_{hf}^{dip}. Whereas only s electrons contribute to the Fermi contact term, electronic states with $l \neq 0$ contribute to the latter terms. In scalar or non–relativistic calculations, the orbital angular momentum is quenched and H_{hf}^{orb}=0; however, when spin–orbit is included, this term can be non–vanishing. In our case, the p ($l = 1$) contribution to the orbital moment is negligible ($<10^{-3}$ μ_B) and the orbital term will be therefore evaluated only for $l = 2$ (d states). The dipolar contribution is normally small in bulk systems and is therefore neglected.

In Table II, we report our calculated values for the core and valence contributions to the Fermi contact hyperfine field, along with the orbital and total contributions, compared with experimental values. The dominant exchange polarization of the core electrons has to be taken into account, showing the need for an all–electron method[11] when dealing with hyperfine fields. As discussed in previous theoretical work for transition metals,[22] in Mn_5Ge_3 the separation of the negative core and positive valence contributions to the Fermi contact hyperfine field highlights these two opposite terms (cf. Table II). The large negative core contribution can be attributed to the attraction of the majority spin electrons towards the spatial region of the spin–polarized d shell[22] which produces the excess of minority spin electrons at the nucleus. In order to evaluate the effects of a different parametrization for the exchange–correlation potential, we compare the Fermi contact term within LSDA and GGA. The total (core+valence) contribution is very similar; however, both the separate core and valence terms have a larger magnitude within GGA. Note that the core polarization per unit spin moment for Mn 1 and Mn 2 in both LDA and GGA is constant - as is expected from the exchange polarization mechanism but with a somewhat different constant, namely ~ 130 kG/μ_B and ~ 140 kG/μ_B within LSDA and GGA, respectively. These values are pretty similar to the values obtained for the Mn–based Heusler compounds[24] ($\sim$ 140 kG/μ_B within LSDA and $\sim$ 150 kG/μ_B within GGA).

As far as the orbital contribution is concerned, we point out that this term is, as expected, much smaller than the Fermi–contact term and very small, because the unquenched orbital moment is so small, as is usual for Mn. Its magnitude could be slightly underestimated due to the well–known failure of SDFT in determining orbital magnetic moment; however, this error is expected not to dramatically change the final value of the total hyperfine field. In particular, we point out that the inclusion of the (positive) orbital term improves (worsens) the agreement with experiment in the case of Mn1 (Mn2). In

TABLE II: GGA calculated Fermi contact hyperfine fields broken down into the core ($H_{hf}^{ct,core}$) and valence ($H_{hf}^{ct,val}$) contributions (values in parenthesis denote LSDA calculated values). The total Fermi contact hyperfine fields ($H_{hf}^{ct,tot}$), the average $< r^{-3} >$ for the d states and the orbital hyperfine field (H_{hf}^{orb}) are also shown. The total hyperfine field $H_{hf}^{t} = H_{hf}^{ct,tot} + H_{hf}^{orb}$ is compared with available experimental data (magnitude of H_{hf}^{exp})[20]. Values of hyperfine fields ($< r^{-3} >$) are expressed in kOe (a_0^{-3}, where a_0 is the Bohr radius).

	$H_{hf}^{ct,core}$	$H_{hf}^{ct,val}$	$H_{hf}^{ct,tot}$	$< r^{-3} >$	H_{hf}^{orb}	H_{hf}^{t}	$\lvert H_{hf}^{exp} \rvert$
Mn1	-316	111	-205	2.14	12.9	-192	195
	(-279)	(76)	(-203)				
Mn2	-459	107	-352	2.18	9.5	-342	399
	(-417)	(70)	(-347)				

fact, by means of zero–field NMR and specific heat measurements, the magnitude of the experimental effective nuclear fields were determined as 195 kOe at the 4(d) Mn site and 399 kOe at the 6(g) Mn site[20]. The agreement of the calculated values ($H_{hf}^{tot}(\mathrm{Mn}_1)$ = -192 kOe and $H_{hf}^{tot}(\mathrm{Mn}_2)$ = -342 kOe) with experiments is seen to be reasonably good.

FERMI VELOCITIES AND DEGREE OF SPIN–POLARIZATION

Since Mn_5Ge_3 has been suggested as a potential spin-injector, it is useful for device applications to give information about transport properties, in terms of Fermi velocities and spin-polarization.

Recall that various definitions of spin–polarization P have been proposed, each of them to be used in different regimes[25]. The most natural and popular definition involves the DOS at E_F and is probed, for example, in spin–polarized photoemission measurements:

$$P_0 = [\mathrm{N}_\uparrow(E_F)\text{-}\mathrm{N}_\downarrow(E_F)]/[\mathrm{N}_\uparrow(E_F)+\mathrm{N}_\downarrow(E_F)]$$

However, in transport measurements (see for example Andreev reflection[26]), Fermi velocities are of course relevant quantities and should therefore be involved in the spin–polarization definition[25]. In particular, for low resistance ballistic contacts, the appropriate definition is:

$$P_1 = (< N(E_F)\cdot v_F >_\uparrow - < N(E_F)\cdot v_F >_\downarrow)/(< N(E_F)\cdot v_F >_\uparrow + < N(E_F)\cdot v_F >_\downarrow)$$

whereas for large barrier and/or diffusive current the correct definition is:

$$P_2 = (< N(E_F)\cdot v_F^2 >_\uparrow - < N(E_F)\cdot v_F^2 >_\downarrow)/(< N(E_F)\cdot v_F^2 >_\uparrow + < N(E_F)\cdot v_F^2 >_\downarrow)$$

where <> denotes the Fermi surface average.

In Figure 5 we show our GGA-calculated in-plane (perpendicular to the c axis) and out-of-plane (parallel to the c axis) velocities as a function of energy.

Moreover, in the upper part of Table III, the corresponding quantities evaluated at the E_F are reported, along with plasma frequencies. According to these values, we have calculated the P_0, P_1 and P_2 values (the latter two for different in-plane and out-of-plane directions) reported in Table III (lower part). Due to the numerical uncertainties (related to the **k**-point sampling, wave function cut-offs, etc.), we estimate an error on the spin–polarization of ±5-10 %. Within this error, our values are consistent with similar values recently obtained using a different DFT method and slightly different lattice parameters.[9]

As pointed out in the discussion of the electronic properties, the Mn heavy d bands in the majority channel are almost fully occupied and the Fermi level also crosses Ge p states, which are light states with an appreciable velocity. On the other hand, in the minority spin-channels, the DOS shows contributions from both Mn heavy d and Ge p states. As clearly shown in Table III, the Fermi DOS in the minority spin–channel is larger - by a factor of ∼2 - than in the majority spin–channel, whereas the Fermi velocities (both in–plane and out–of–plane) are larger by a factor of ∼3 for majority spins. This leads to a negative spin-polarization P_0, but to a positive current (see positive values of P_1), as also noted in 3d metals.[25] As for the plasma frequencies, we point out that there are only slight differences between in-plane and out-of-plane

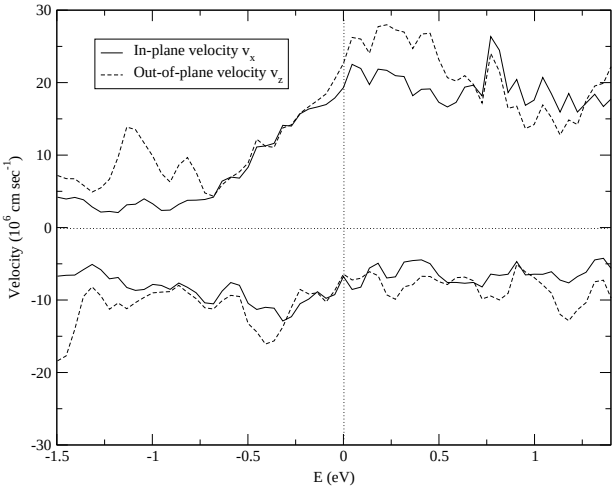


FIG. 5: In-plane (solid) and out-of-plane (dashed) velocities as a function of energy for majority and minority spin electrons (positive and negative y axis, respectively).

TABLE III: Upper part: GGA-calculated relevant quantities at E_F for up and down spin-channels (first and second line, respectively): Density of states ($N(E_F)$, in states/eV), in-plane velocity ($v_{F\parallel}$, in 10^6 cm/sec), out-of-plane velocity ($v_{F\perp}$, in 10^6 cm/sec), in-plane plasma frequency ($\omega_{p\parallel}$, in eV) and out-of-plane plasma frequency ($\omega_{p\perp}$, in eV). Spin–orbit coupling is not included. Lower part: Degree of spin–polarization (DSP) as measured in photoemission measurements (P_0), ballistic transport (in–plane and out–of–plane, $P_{1\parallel}$ and $P_{1\perp}$, respectively) and diffusive transport (in-plane and out-of-plane ($P_{2\parallel}$ and $P_{2\perp}$, respectively.) - see text for definitions. For comparison, we also show similar quantities obtained for ferromagnetic hcp Co.

	Compound	$N(E_F)$	$v_{F\parallel}$	$v_{F\perp}$	$\omega_{p\parallel}$	$\omega_{p\perp}$
Spin-up	Mn_5Ge_3	3.3	19.3	22.6	2.0	2.4
Spin-down		7.9	6.7	6.4	1.1	1.1
Spin-up	Co	0.3	47.9	38.2	5.0	4.0
Spin-down		1.5	14.0	16.4	3.3	3.8

	Compound	P_0	$P_{1\parallel}$	$P_{1\perp}$	$P_{2\parallel}$	$P_{2\perp}$
DSP	Mn_5Ge_3	-41%	8%	18%	54%	67%
	Co	-67%	-19%	-37%	40%	4%

calculated values, whereas larger differences between minority and minority spins emerge: $\omega_p^{\uparrow}$ is about two times larger than $\omega_p^{\downarrow}$.

As shown in Figure 5, the anisotropy of the in–plane with respect to the out–of–plane velocity is quite evident: although the behavior as a function of energy is overall similar, they slightly differ in the case of majority spins, at about -1eV and in the relevant energy range around the Fermi level (from -0.2 to 0.5 eV in the majority channel). Moreover, as shown in Table III, the different definitions of spin polarizations result in largely differing values. Both the anisotropy as well as the differences among P_0, P_1 and P_2 should help in exploiting this compound for spin–injections purposes in the most appropriate transport regime and along the most favorable growth direction. In particular, we remark that with $P_{2\perp} \sim 70\%$, most of the current along the c axis in the diffusive (Ohmic) regime is therefore carried by majority spins. Of course, this picture might be modified in the presence of a junction (such as Mn_5Ge_3/Ge), where interface states can modify the electronic structure and velocities with respect to the ideal bulk situation considered here.

Finally, it is useful to compare calculated spin-injection efficiencies and Fermi velocities for Mn_5Ge_3 with those obtained for ferromagnetic hcp Co[27], a widely used material in high density magnetic recording media. Our results are shown in Table III. Interestingly, the cobalt Fermi velocities (and related plasma frequencies) are larger by a factor of 2-3 compared to Mn_5Ge_3 , also showing a larger anisotropy. As far as the Co DSP is concerned, we remark that, similarly to Mn_5Ge_3 , P_0 is negative; however, P_1 - both in–plane and out–of–plane - is also negative, at variance with Mn_5Ge_3. As a final remark, we observe that the Co spin polarization in the ballistic regime is slightly higher than in Mn_5Ge_3 , whereas it is definitely lower in the diffusive regime, holding promise for Mn_5Ge_3 as an efficient spin–injector.

X–RAY ABSORPTION AND MAGNETIC CIRCULAR DICHROISM

The formalism within band theory to calculate the cross section for the absorption of incident light is discussed in Ref.28 and is briefly reviewed here. For dipole–excited transitions, the cross section can be obtained as:

$$\sigma_n(E) = \int_{\Omega_{BZ}} | < \Psi_c|p|\Psi_v > |^2 \delta(E - (E_v - E_c))d\mathbf{k} \quad (4)$$

where $n = z, \pm$ represents the photon polarization (i.e. incident light polarized vertically along the direction of magnetization (z) or left- ($+$) or right–circularly ($-$) polarized), p is the momentum operator, Ψ_c and Ψ_v (E_c and E_v) denote initial core and final valence states (eigenenergies), respectively. Therefore, the X-ray magnetic circular dichroism (XMCD) can be obtained as $\sigma_m = \sigma_+ - \sigma_-$, whereas the X-ray absorption spectrum (XAS) is calculated as $\sigma_t = \sigma_+ + \sigma_- + \sigma_0$ (σ_0 denotes the absorption cross section for incident light polarized vertically along the direction of magnetization, here chosen as coincident with the z hexagonal axis). Starting from the converged FLAPW ground state, the spin-orbit coupling (SOC) was treated in a second variational way[16] to obtain the XAS and XMCD spectra, using up to 432 **k**-points in the full Brillouin zone. We used a 0.25 eV Lorentzian broadening to smooth the calculated spectra, in order to take lifetime effects into account (see below).

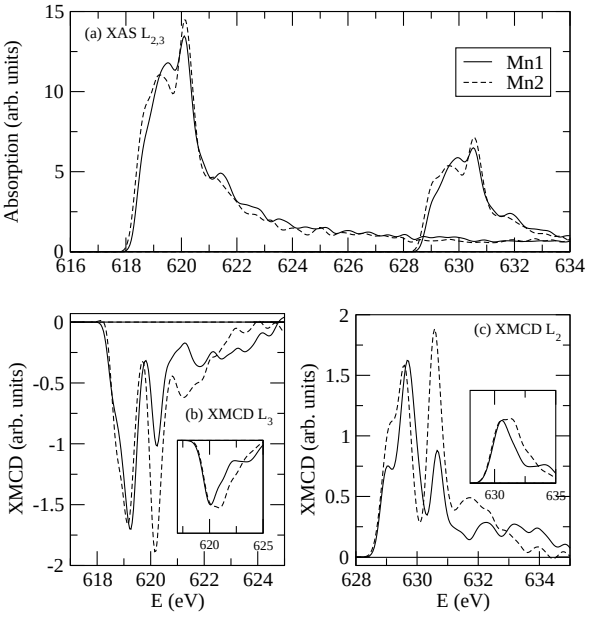


FIG. 6: (a) $L_{2,3}$ X-ray absorption; (b) L_3 X-ray MCD; and (c) L_2 X-ray MCD. The insets in panels (b) and (c) show MCD spectra convoluted with an energy broadening of 0.7 eV. In all panels, the solid (dashed) line shows the contribution of the Mn1 (Mn2) site.

The energy dependence of $L_{2,3}$ σ_m and σ_t are shown in Figure 6 for the two Mn atomic types. As is usual for $3d$ metals,[28] and pointed out above in the PDOS discussion, most of the majority spin bands are located below E_F, so that photon induced transitions occur mainly to the unoccupied minority spin–bands. We haven't included any self–energy correction, so we expect the calculated binding energy of the $2p$ states to be underestimated by several tenths of an eV. The energy difference between the L_2 and L_3 edge represents the size of the spin-orbit splitting of the $2p$ core states, and is usually found to be in good agreement with experiment. For Mn_5Ge_3 it is estimated to be $\Delta_{SOC}^{2p} = 10.4$ eV. This value is similar to other theoretical results for Mn based alloys, such as the Heusler PtMnSb and NiMnSb[29], as

well as to other experimental data obtained for DMS[30]. As expected from the quite low symmetry of the hexagonal lattice (and the related difference of the out–of–plane z direction compared to the in–plane x, y direction), σ_0 is quite different from $\frac{1}{2}(\sigma_+ + \sigma_-)$ (not given in Figure 6). The XAS spectrum shows tails extending to high energy (>10-15 eV) with respect to the main absorption peaks, whereas the XMCD becomes almost negligible at 5-7 eV above the absorption edge. For the energy broadening value used (0.25 eV), both the absorption and dichroism spectra show a quite rich structure; in particular, the XAS and - even more markedly - the XMCD spectra show a double peak structure (related to the peculiar features in the unoccupied density of states, see Fig.2 (b) and (c)), followed by a smaller bump at about 3.5 eV above the absorption edge. As far as the comparison between Mn1 and Mn2 is concerned, we remark that the XAS spectrum shows similar features, whereas the XMCD shows different amplitudes of the second peak, which is more marked in Mn2 compared to Mn1. This difference in the XMCD intensity is consistent with the larger Mn2 magnetic moment compared to Mn1. Since the broadening used (0.25 eV) is lower than the common experimental resolution, we also show in the insets of Fig.6 (b) and (c) the same XMCD spectra obtained using a Lorentzian broadening equal to 0.7 eV; in this case, the double–peak feature cannot be resolved, whereas the larger amplitudes observed for Mn2 compared to Mn1 in the high energy range is still evident.

To further investigate this issue, we recall that some important magneto-optical sum rules have been derived in recent years, which relate the integrated signals over the spin–orbit split core edges of the unpolarized XAS and of circular dichroism to ground–state orbital and spin magnetic moments[31, 32, 33, 34]. The orbital and spin sum rules are expressed as:

$$< l_z >= \frac{2 I_m N_h}{I_t} \tag{5}$$

$$< s_z >= \frac{3 I_s N_h}{I_t} - 7 < T_z > \tag{6}$$

$$I_m = \int [(\sigma_m)_{L_3} + (\sigma_m)_{L_2}] d\epsilon \tag{7}$$

$$I_s = \int [(\sigma_m)_{L_3} - 2(\sigma_m)_{L_2}] d\epsilon \tag{8}$$

$$I_t = \int [(\sigma_t)_{L_3} + (\sigma_t)_{L_2}] d\epsilon \tag{9}$$

where N_h is the number of holes in the d band, $N_h = 10 - n_{3d}$ (with n_{3d} determined by the d projected density of states inside each atomic sphere). T_z is the z component of the magnetic dipole operator:

$$T_z = 1/2 \; [\boldsymbol{\sigma} \text{ - } 3 \; \hat{\mathbf{r}} (\hat{\mathbf{r}} \cdot \boldsymbol{\sigma})]_z$$

TABLE IV: Orbital and spin magnetic moments as determined from sum–rules (SR) and self-consistently (SC) for Mn1 and Mn2 atoms along with their ratio.

	μ^l		μ^s		μ^l/μ^s	
	SR	SC	SR	SC	SR	SC
Mn1	0.03	0.05	1.9	2.07	0.015	0.024
Mn2	0.02	0.035	2.4	3.16	0.01	0.01

with $\boldsymbol{\sigma}$ denoting the vector of Pauli matrices and is related to the non-spherical charge and spin density. T_z is vanishing for cubic systems, whereas it is not necessarily negligible in hexagonal systems. However, preliminary calculations suggest that T_z is pretty small (at most of the order of 0.03) and is therefore neglected here. The orbital and spin magnetic moments are $\mu^l = -\mu_B < l_z >$ and $\mu^s = -\mu_B < s_z >$, respectively. Their ratio, as derived from sum rules, reads as:

$$\frac{\mu^l}{\mu^s} = \frac{< l_z >}{< s_z >} = \left[\frac{3 \, I_s}{2 \, I_m} - \frac{7 < T_z > I_t}{2 \, I_m \, N_h} \right]^{-1} \tag{10}$$

Experimentally, since $< T_z >$ is very hard to access, it is generally neglected when considering sum rules; in this case the experimental uncertainties - related to fixing somehow the number of holes N_h or to calculating I_t - drop out. It has therefore been suggested [35] that an accurate estimate of the μ^l/μ^s ratio can be obtained from the $2I_m/3I_s$ ratio.

In Table IV we report our calculated values for the orbital and spin magnetic moments, as well as their ratio, as determined from sum rules (SR) for Mn1 and Mn2 atoms. For comparison, we also report the same values as self-consistently calculated (cfr. Table I). As expected, the general trends of spin and magnetic moments for Mn1 and Mn2 atoms are qualitatively well reproduced. However, quantitatively, the SR magnetic moments are generally underestimated with respect to the self-consistently calculated values (ranging from ∼10 percent in the case of spin magnetic moments up to 40 % in the case of the small orbital moments). This has been ascribed[33] to the several approximations made in deriving the sum rules[36], among which the most serious are *i*) ignoring the interatomic hybridization, *ii*) neglecting the $p \rightarrow s$ transitions[33], and *iii*) ignoring the exchange splitting of core levels. Therefore, first–principles calculations of both XMCD spectra and ground–state magnetic moments are crucial for a careful study of the Mn_5Ge_3 compound and, eventually, for a quantitative interpretation of future experimental results.

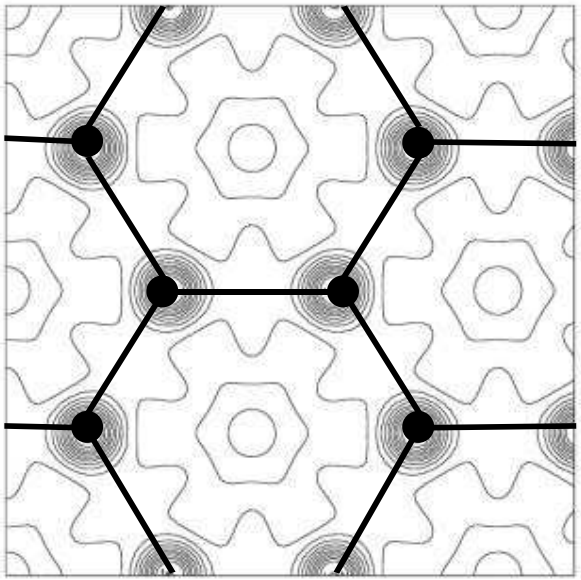
SUMMARY

In the search for new compounds to be used for efficient spin–injection in spintronic devices and following the re-

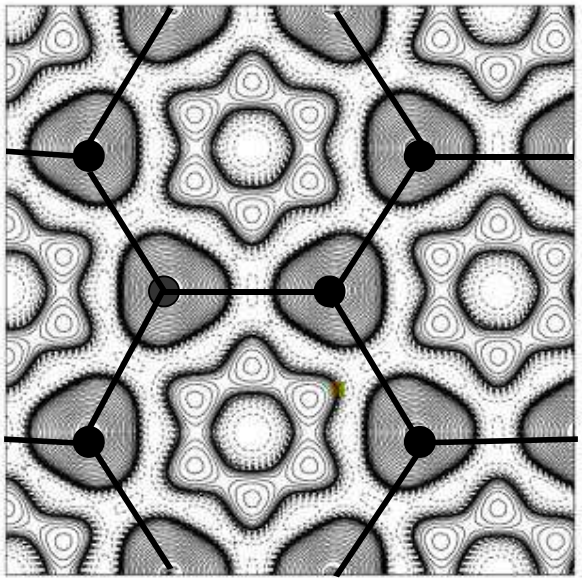
cent suggestion of Mn_5Ge_3/Ge(111) system as a promising system, we have presented a careful first-principles FLAPW investigation of the electronic, transport, magnetic and magneto–optical properties of bulk Mn_5Ge_3. Our results show that the two Mn sites have different magnetic moments, leading to a total magnetization of 26 μ_B per unit cell; the conducting character is strongly metallic with states around the Fermi level essentially due to Mn-Mn interactions. Our theoretical predictions were carefully analyzed in terms of the underlying electronic and magnetic structure and shown to be in excellent quantitative and qualitative agreement with available experimental results. The most favorable condition for spin–injection purposes is predicted to be in the diffusive regime along the hexagonal c axis, where a rather high spin-polarization is obtained.

We thank Prof. Ruqian Wu and Prof. Sandro Massidda for assistance provided with the calculation of the magnetic dipole operator and spline fitting procedure, respectively. Useful discussions with Dr. Steven C. Erwin are gratefully acknowledged. Work in L'Aquila supported by INFM through Iniziativa Trasversale Calcolo Parallelo and PAIS-GEMASE project.

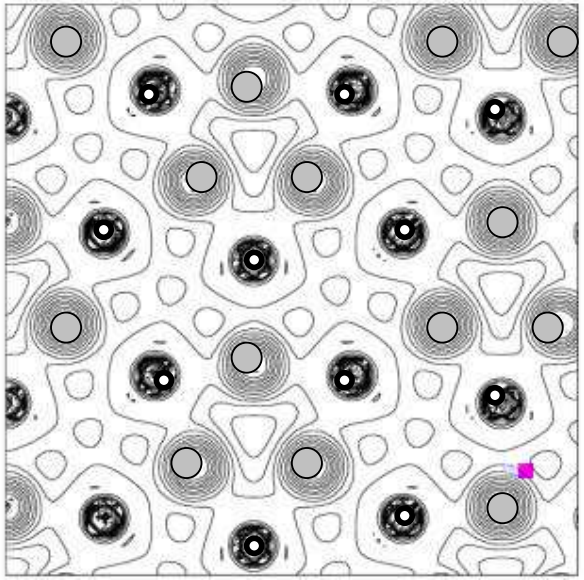
[1] T. Dietl, H. Ohno, F. Matsukura, J. Cibert and D. Ferrand, Science **287**, 1019 (2000).
[2] I. Zutic, J. Fabian and S. Das Sarma, Rev. Mod. Phys. **76**, 323 (2004).
[3] Y. D. Park, A. T. Hanbicki, S. C. Erwin, C. S. Hellberg, J. M. Sullivan, J. E. Mattson, T. F. Ambrose, A. Wilson, G. Spanos, and B. T. Jonker, Science **295**, 651 (2002).
[4] Y. D. Park, A. Wilson, A.T. Hanbicki, J.E. Mattson, T. Ambrose, G. Spanos, and B. T. Jonker, Appl. Phys. Lett. **78**, 2739 (200 1).
[5] T. Matsui, M. Shigematsu, S. Mino, H. Tsuda, H. Mabuchi and K. Morii, J. of Magn. Magn. Mat. **192**, 247 (1999).
[6] Y. Tawara and K. Sato, Proc. Phys. Soc. Japan **18**, 773 (1963).
[7] J. B. Forsyth and P.J. Brown, J. Phys.: Condens. Matter **2**, 2713 (1990).
[8] C. Zeng, S.C.Erwin, L.C.Feldman, A.P.Li, R. Jin, Y. Song, J.R.Thompson and H.H.Weitering, Appl. Phys. Lett. **83**, 5002 (2003).
[9] R. P. Panguluri, C. Zeng, H. H. Weitering, J. M. Sullivan, S. C. Erwin and B. Nadgorny, cond-mat/0407001.
[10] M. Gajdzik, C. Sürgers, M. Kelemen and H. v. Löhneysen, J. Mag. Magn. Mat. **221**, 248 (2000).
[11] E. Wimmer, H. Krakauer, M. Weinert and A. J. Freeman, Phys. Rev.B **24**, 864 (1981); H.J.F.Jansen and A.J.Freeman, Phys. Rev. B **30**, 561 (1984).
[12] J. P. Perdew, K. Burke and M. Ernzerhof, Phys. Rev. Lett. **77**, 3865 (1996).
[13] A. Continenza, S. Picozzi, W. T. Geng and A. J. Freeman, Phys. Rev. B **64**, 085204 (2001).
[14] U. von Barth and L. Hedin, J. Phys. C **5**, 1629 (1972).
[15] H.J.Monkhorst and J.D.Pack, Phys. Rev. B **13**, 5188 (1976).
[16] A. H. Mac Donald, W. E. Pickett and D. D. Koelling, J. Phys.C **13**, 2675 (1980).
[17] D.D.Koelling and J.H.Wood, J. Comput. Phys. **67**, 253 (1986).
[18] A. Stroppa, S. Picozzi, A. Continenza and A.J.Freeman, Phys. Rev. B **68**, 155203 (2003).
[19] J.B. Forsyth and P.J.Brown, Proc. Int. Magnetism Conf. (Nottingham) (London: The Physical Society), p.524.
[20] R.F. Jackson, R.G. Scurlock, D.B. Utton and E. M. Wray, Proc. Phys. Soc. **85**, 127 (1965).
[21] G. Kappel, G. Fischer and A. Jaéglé, Phys. Lett. **45A**, 267 (1973); G. Kappel, G. Fischer and A. Jaéglé, Phys. Status Solidi **34**, 691 (1976).
[22] A. J. Freeman and R. E. Watson, in *Magnetism*, edited by G. T. Rado and H. Shul (Academic, New York, 1965) Vol. IIA; R.E. Watson and A.J.Freeman, Phys. Rev. **123**, 2027 (1961).
[23] A. Abragam and M.H.L.Price, Proc. R. Soc. London Ser. A **205**, 135 (1951).
[24] S. Picozzi, A. Continenza and A.J.Freeman, Phys. Rev. B **66**, 094421 (2002).
[25] I.I.Mazin, Phys. Rev. Lett. **83**, 1427 (1999).
[26] R. J. Soulen, J. M. Byers, M. S. Osofsky, B. Nadgorny, T. Ambrose, S. F. Cheng, P. R. Roussard, C. T. Tanaka, J. Nowak, J. S. Moodera, A. Barry and J. M. D. Coey, Science **282**, 85 (1998).
[27] The hcp Co was simulated using the experimental lattice constants $a = 2.51$ Åand $c = 4.07$ Å.
[28] R. Wu, D. Wang and A. J. Freeman, J. of Mag. Mag. Mat. **132**, 103 (1994).
[29] I. Galanakis, S. Ostanin, M. Alouani, H. Dreyssé and J. M. Wills, Phys. Rev. B **61**, 4093 (2000).
[30] Y. Ishiwata *et al.*, Phys. Rev. B **65**, 233201 (2002); K. Cho *et al.*, Phys. Rev. B **63**, 155203 (2001).
[31] B. T. Thole, P. Carra, F. Sette, and G. Van der Laan, Phys. Rev. Lett. **68**, 1943 (1992).
[32] P. Carra, B. T. Thole, M. Altarelli, and X. Wang, Phys. Rev. Lett. **70**, 694 (1993).
[33] R. Wu and A. J. Freeman, Phys. Rev. Lett. **73**, 1994 (1994); R. Wu, D. Wang and A. J. Freeman, Phys. Rev. Lett. **71**, 3581 (1993); R. Wu, D. Wang and A. J. Freeman, J. Mag. Magn. Mat. **132**, 103 (1994).
[34] A. Ankudinov and J. J. Rehr, Phys. Rev. B **51**, 1282 (1995); G. Y. Guo, *ibid.* 57, 10295 (1998).
[35] C. T. Chen, Y. U. Idzerda, H. J. Lin, N. V. Smith, G. Meigs, E: Chaban, G. H. Ho, E. Pellergin, and F. Sette, Phys. Rev. Lett. **75**, 152 (1995).
[36] H. Ebert, Rep. Prog. Phys. **59**, 1665 (1996).



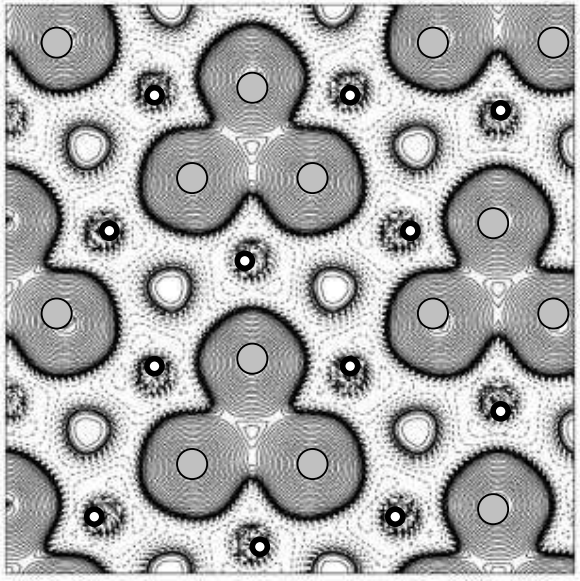
(a)



(b)



(c)



(d)

Fig.4 –